ACS OMEGA

Open Access

http://pubs.acs.org/journal/acsodf

Article

Effects of $\pi-\pi$ Stacking on Shale Gas Adsorption and Transport in Nanopores

Fuye Chen, Jiaxuan Tang, and Jiang Wang*

Cite This: *ACS Omega* 2023, 8, 46577−46588

Read Online

ACCESS | Metrics & More | Article Recommendations | Supporting Information

ABSTRACT: The $\pi-\pi$ interaction is a prevalent driving force in the formation of various organic porous media, including the shale matrix. The configuration of $\pi-\pi$ stacking in the shale matrix significantly influences the properties of shale gas and plays a crucial role in understanding and exploiting gas resources. In this research, we investigate the impact of different $\pi-\pi$ stacking configurations on the adsorption and transport of shale gas within the nanopores of the shale matrix. To achieve this, we construct kerogen nanopores using $\pi-\pi$ stacked columns with varying stacking configurations, such as offset/parallel stacking types and different orientations of the stacked columns. Through molecular dynamics simulations, we examined the adsorption and transport of methane within these nanopores. Our findings reveal that methane exhibits stronger adsorption in smoother nanopores, with this adsorption remaining unaffected by the nanoflow. We observe a heterogeneous distribution of the 2D adsorption free energy, which correlates with the specific $\pi-\pi$ stacking configurations. Additionally, we introduce the concept of "directional roughness" to describe the surface characteristics, finding that the nanoflow flux increases as the roughness decreases. This research contributes to the understanding of shale gas behavior in the shale matrix and provides insights into nanoflow properties in other porous materials containing $\pi-\pi$ stackings.

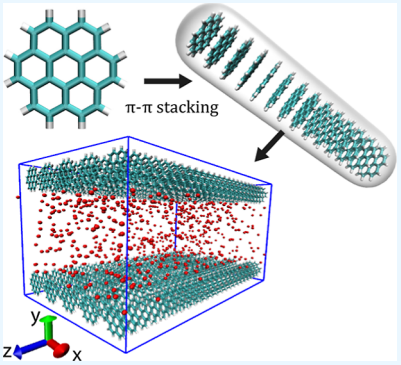

1. INTRODUCTION

The escalating global demand for energy and fuels has led to the gradual emergence of shale gas as a paramount energy source and a dominant form of fossil fuel.[1−4] Primarily comprising methane, shale gas offers several advantages, including its abundant storage capacity and relatively cleaner emissions compared to other fossil fuels.[5,6] Shale gas in place is mostly stored in the organic porous media, known as kerogen,[7−11] which is formed through intricate processes involving the burial of organic material deep underground, including pyrolysis and thermal maturation. These processes give rise to the development of a highly complex structure and exceptionally large size for individual kerogen molecules.[10]

Various experimental techniques, including small-angle neutron scattering,[12,13] mercury intrusion,[14,15] atomic force microscopy,[16] and scanning electron microscopy,[17] have demonstrated that the kerogen matrix exhibits a porous structure characterized by nanopores and nanochannels ranging in size from 1 to 100 nm.[15,18] These nanopores and nanochannels play a critical role, as most methane molecules are adsorbed onto their surfaces. Consequently, comprehending the adsorption and transport behavior of methane within these nanopores and nanochannels is of utmost importance for gas exploitation engineers.[19−22]

Recent experimental and numerical studies indicate that there are plenty of $\pi-\pi$ stacked aromatic structures in kerogen.[23−27] For instance, organic geochemical measurements have revealed that aliphatic chains are folded with no specific order, while large aromatic units are stacked.[23] Lísal and co-workers used molecular dynamics (MD) simulations to generate realistic kerogen and nanopore walls and demonstrated that the stacked aromatic kerogen structure significantly affects the interaction between kerogen and methane.[24] Moreover, $\pi-\pi$ stacking serves as a crucial driving force for the formation of various other porous media and is found in a wide range of organic and biological materials.[28−32]

The adsorption and transport properties of methane in nanopores are profoundly influenced by the characteristics of the pore surface, including $\pi-\pi$ stacking structures and the stacking orientation. However, investigating the intricate details of methane behavior at such a small scale remains challenging.[33−38] MD simulations have emerged as a valuable tool for exploring the nanoscale behavior of methane molecules in the porous shale matrix.[39−49]

MD have been extensively employed to investigate the adsorption and transport behavior of methane in nanopores, exploring various aspects such as nanochannel surface roughness,[50] nanopore cross-sectional shape,[51] and nanochannel with

Received: July 28, 2023
Revised: November 20, 2023
Accepted: November 22, 2023
Published: December 2, 2023

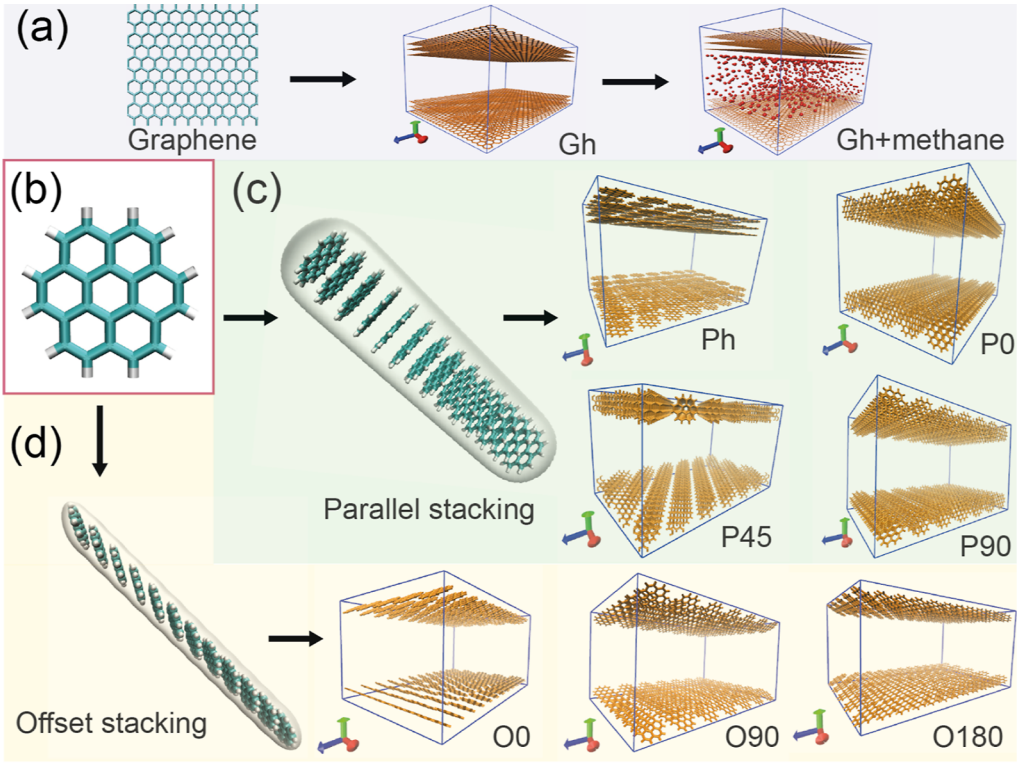

Figure 1. (a) Graphene sheets assembled into a three-layer nanoslit (atoms in the shale matrix are colored in orange) and then methane (red balls) molecules are inserted into the nanoslit. **Gh** is short for "Graphene horizontal", meaning that the surface of the graphene sheet is horizontal relative to the nanopore wall surface. Three axes are colored as *x*/red, *y*/green, and *z*/blue. (b) The aromatic unit with seven benzene rings highlighted in red box. (c) Aromatic units are parallel stacking into straight columns, and then the stacked column could form 4 types of nanoslits with different column orientations. **Ph** represent "Parallel horizontal", similarly to that of **Gh**. In **P0**, **P45**, and **P90**, their column axles have angles of 0, 45, and 90° with respect to the *z* axis, respectively. (d) Aromatic units are offset stacking to each other, and then, the stacked column could form three types of nanoslits based on the column axle orientation. **O0**, **O90**, and **O180** mean that the column axle has angles of 0, 90, and 180° with respect to the *z* axis.

functional groups.[52,53] Additionally, studies have examined the arrangement of carbon atoms and graphenes on nanopore walls, revealing their influence on the density and velocity distribution of methane flows.[54,55] Notably, researchers have introduced a novel "cuter atom" method to generate more realistic nanopores, uncovering heterogeneous methane adsorption behavior in these realistic models.[56,57] Other methods such as Monte Carlo simulation have also been applied to understand the properties of methane in a realistic kerogen matrix.[58]

$\pi-\pi$ stacking refers to the one-dimensional columnar arrangement of stacked aromatic molecular units through $\pi-\pi$ interactions,[32,59−61] as illustrated in Figure 1. The presence of $\pi-\pi$ stacking has been found to have a significant influence on the interaction between kerogen and methane.[24] However, to the best of our knowledge, no systematic research has been conducted to investigate the specific impact of $\pi-\pi$ stacking on the methane adsorption and transport behavior in nanopores.

In this study, our focus is on analyzing the structure of kerogen nanochannels with various $\pi-\pi$ stacked configurations. Specifically, we examine factors such as the orientation of the stacking axle, type of stacking (parallel or offset), and nanopore sizes. To achieve this, we constructed an artificial nanopore using exclusively stacked columns. Subsequently, we employed MD simulations to investigate the behavior of methane within these nanopores. This approach enables us to quantitatively explore the impact of stacking types and orientations on shale gas adsorption and transport and block out the impact from other factors such as functional groups or the shape of the nanopore. The findings from this research will be useful for enhancing our understanding of shale gas properties within shale matrix and provide valuable insights into nanoflow phenomena in other porous media consisting of $\pi-\pi$ stackings, such as the nanochannel formed in discotic liquid crystals.[62,63]

2. METHODS

2.1. Nanoslit Structures. The kerogen nanopore is constructed as shown in Figure 1a, first we use a three-layered graphene sheet to form a nanoslit, the surface of the graphene lays horizontally and is parallel to the slit, and this nanochannel is denote as **Gh** short for "graphene horizontal", as a comparison structure, **Gh** is quite smooth. Previous studies found that the adsorption energy of methane onto graphene is similar to that in real shale, making graphene a suitable model for kerogen walls.[64]

It needs to be pointed out that even though we term the artificial nanopore/slit/channel we constructed in this paper as 'kerogen nanopore/slit/channel', it is still far from a realistic kerogen structure, as it misses the disordered complexity and functional groups realistic kerogen have. The aim of this research is to investigate how different $\pi-\pi$ stacking configurations will impact shale gas adsorption and transport, so a simple ordered artificial nanoslit structure is only considered to block out the impact from other factors.

Several studies indicate that the aromatic parts of kerogen are stacked rings with the dominant ring size of 2×2 and 3×3,[26,27] meaning that there are 4−9 benzene rings in the aromatic core. In this article, we choose a symmetrical unit structure with a size

https://doi.org/10.1021/acsomega.3c05522
ACS Omega 2023, 8, 46577−46588

of 7 ($C_{24}H_{12}$), as shown in the red box in Figure 1b. The graphene unit could further form parallel or offset stacked columns, as shown in Figure 1c,d, and the distance between adjacent units is set to 0.335 nm.[65]

Then the parallel stacked column could form a nanoslit with the unit surface lays horizontally (denote as **Ph** short for 'parallel stacking horizontal'), or with the column axle aligning with z axis, named as **P0**, since the angle between the column axle and the z axis being 0°. Similarly, the angles between the column axle and the z axis can be 45 and 90°, denoted as **P45** and **P90**, respectively.

As to the offset stacking type, the axle of the stacked column could be arranged along the z axis, with the angle of 0° (named as **O0** short for "offset 0°"); perpendicular to the z axis, with the angle of 90° (**O90**), and against the z axis, with the angle of 180° (**O180**). Note that if the aromatic units are offset stacked, **O0** and **O180** are different, since the flow is moving in the z direction. The visualization of all types of nanoslit from x, y, and z directions could be found in the Supporting Information.

2.2. MD Simulation. All simulations are conducted using large-scale Atomic/Molecular Massively Parallel Simulator (LAMMPS),[66,67] in a box with periodic boundary conditions in x, y, and z directions. Methane molecules were randomly inserted into the slit at the start of the simulation. Simulations were performed under the NVT ensemble, where the temperature is set to 350 K and is coupled with a Nose−Hoover thermostat, and an appropriate number of methane molecules is chosen to make the pressure at 20 MPa. During the simulation, kerogen units were kept frozen, while only the methane molecules were allowed to move. The simulation integration step time is 2.0 fs; a 1.0 ns equilibrium run is first conducted, followed by a 10.0 ns production run.

The molecular topology of the kerogen unit was generated using the automated topology builder (http://atb.uq.edu.au).[68−70] The methane molecule was modeled as a single united atom. The slit structure was first constructed using Gromacs[71] and in-house code, and then transferred to a LAMMPS structure file using the Gro2lam package.[72]

There are three types of atoms in our research: C_{Aro} is the aromatic carbon atom in the kerogen unit, H is the hydrogen atom at the edge of kerogen unit, and CH_4 is the single united atom that represents a methane molecule. The interaction between atom type i and j was determined using the Lennard-Jones function

$$V_{LJ}=4\epsilon_{ij}\left[\left(\frac{\sigma_{ij}}{r_{ij}}\right)^{12}-\left(\frac{\sigma_{ij}}{r_{ij}}\right)^{6}\right] \quad (1)$$

with a cutoff of 1.2 nm. Values of ϵ_{ij} and σ_{ij} are list in Table 1. When an atom is interacting with another one with the same type, we have $i = j$, $\epsilon_{ii} = \epsilon_i$, and $\sigma_{ii} = \sigma_i$.

If $i \neq j$, then we use geometrical rules to obtain the parameters for the interaction between two different atom types

Table 1. Parameters of the Lennard-Jones Function for Each Atom Type Used in This Research

atom	ϵ (kcal/mol)	σ (Å)	mass (Da)
C_{Aro}	0.07342	3.52053	12.0110
H	0.02828	2.37341	1.0080
CH_4	0.30187	3.70995	16.0430

$$\epsilon_{ij} = \sqrt{\epsilon_i \epsilon_j} \quad (2)$$

$$\sigma_{ij} = \sqrt{\sigma_i \sigma_j} \quad (3)$$

ϵ_{ij} and σ_{ij} parameters were determined based on the Gromos54a7 force field,[73] which is suitable for simulating hydrocarbons and biomolecules. Electrostatic interactions in our system could be ignored since the charged kerogen units were kept frozen, and the methane united atoms were electroneutral. To verify the accuracy of the interaction parameters we used, we have simulated methane gas in the bulk state at T = 350 K, with a pressure of 20 MPa, and compared the density with experimental measurements. The density value from our simulation is 7.295 mol/L, and the experimental value is 7.443 mol/L,[74] and the relative error is 1.99%. The small error indicates that the force field of our model is accurate in capturing properties of methane at high pressures in a nanoslit. For more details of the simulation setups, please refer to the Supporting Information.

Equilibrium MD is conducted to simulate the adsorption of methane onto nanopores, and external field nonequilibrium MD (EF-NEMD) is used to simulate the transport behavior of methane in nanochannel.[47−49] In EF-NEMD, each methane molecule is exerted by a constant force $f = 0.001$(kcal/mol)/Å in the z direction, this external force will add a pressure difference $\Delta P = f \cdot N/A$ to the methane inside the nanoslit in the z direction, where N is the number of methane molecules in the slit, and A is the area of the cross section in the $x-y$ plane.[56]

2.3. Simulation Setups. In this study, we aimed to investigate the impact of multiple factors on the methane behavior in the nanochannel, and to achieve this, we performed 25 simulation runs. In addition to studying the wall structure, we also examined the effect of slit size; there are three sizes: small (slit width of 1.0 nm), medium (slit width of 3.0 nm), and large (slit width of 6.0 nm). The simulation setup parameters are summarized in Table 2. Notably, all simulations were conducted at a temperature of 350 K, and a pressure of 20 MPa, to mimic the shale geological condition deep underground. The target pressure of methane, denoted as P in the table, determined the suitable number of methane molecules. As our simulations were under the NVT ensemble and there was no pressure coupling, the actual pressures fluctuate around the target pressure, and the average pressures we measured from adsorption simulations are listed in Table S2.

3. RESULTS AND DISCUSSION

3.1. $\pi-\pi$ Stacking Affects Shale Gas Adsorption. The 1D methane adsorption probability density $\rho(y)$ over the y axis is calculated, since the wall of nanoslits are in the $x-z$ plan, $\rho(y)$ could capture the interactions between methane and kerogen walls. Figure 2 shows $\rho(y)$ for **Gh**, **Ph**, **P0**, and **O0** with slit sizes s = 10.0, 30.0, and 60.0 Å. The surface of the wall is defined as the layer of the innermost atoms, as indicated by the red dashed line in Figure 2a for type **P0**, under this definition of the wall surface, there will be extra areas in grooves between kerogen units as indicated by the green circle in Figure 2a that can be accessed by a small fraction of methane molecules.

All y coordinates shift to be centered at 0.0. As to **P45** and **P90**, they have different stacked column orientations from **P0**, and this will not impact the methane adsorption behavior because the landscapes of their surfaces are all intrinsically identical to each other if ignoring the column orientation. The

https://doi.org/10.1021/acsomega.3c05522
ACS Omega 2023, 8, 46577−46588

Table 2. Simulation Parameters for Each Run in This Research[a]

ID	wall	size (nm)	box size (nm) $L_x \times Ly \times Lz$	P (MPa)	no. of methane	f ((kcal/mol)/Å)	ID
1	**Gh**	1.0	5.577 × 2.84 × 7.98	20.0	280	0.001	1
2		3.0	5.577 × 4.84 × 7.98	20.0	780	0.001	2
3		6.0	5.577 × 7.84 × 7.98	20.0	1350	0.001	3
4	**Ph**	1.0	5.5 × 2.675 × 7.7	20.0	350	-	4
5						0.001	5
6		3.0	5.5 × 4.675 × 7.7	20.0	750	-	6
7						0.001	7
8		6.0	5.5 × 7.675 × 7.7	20.0	1300	-	8
9						0.001	9
10	**P0**	1.0	5.5 × 3.025 × 8.04	20.0	320	-	10
11						0.001	11
12		3.0	5.5 × 5.025 × 8.04	20.0	650	-	12
13						0.001	13
14		6.0	5.5 × 8.025 × 8.04	20.0	1250	-	14
15						0.001	15
16	**P45**	3.0	5.129 × 5.025 × 8.621	20.0	650	0.001	16
17	**P90**	3.0	5.025 × 5.025 × 7.7	20.0	600	0.001	17
18	**O0**	1.0	5.5 × 2.1 × 8.04	20.0	300	-	18
19						0.001	19
20		3.0	5.5 × 4.1 × 8.04	20.0	700	-	20
21						0.001	21
22		6.0	5.5 × 7.1 × 8.04	20.0	1300	-	22
23						0.001	23
24	**O90**	3.0	5.36 × 4.1 × 7.7	20.0	650	0.001	24
25	**O180**	3.0	5.5 × 4.1 × 8.04	20.0	700	0.001	25

[a]Simulation IDs are list in the first and the last column to help identify simulations. "-" in f column indicate that the external field in z direction is set to 0.

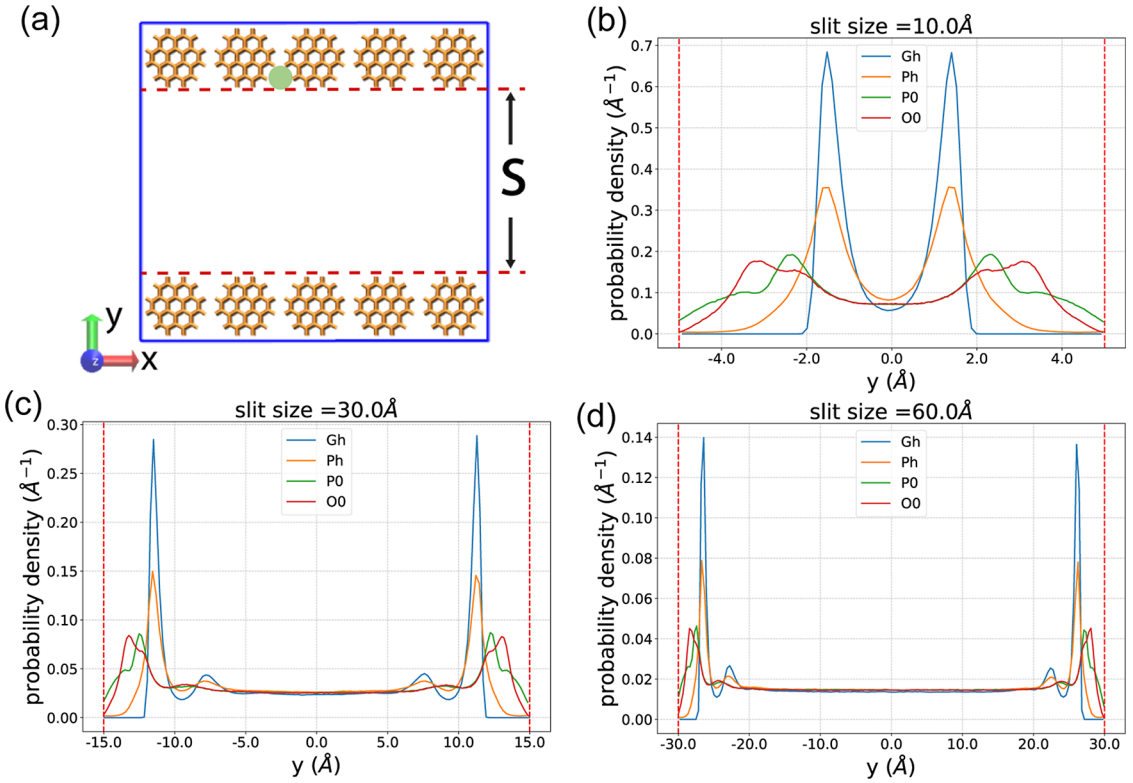

Figure 2. (a): Definition of the wall surface. 1D probability density distribution of methane adsorption over the y axis for slit sizes of (b): 10 Å, (c): 30 Å, and (d): 60 Å.

same to **O90** and **O180**, they will have the same methane adsorption profile to **O0**.

In Figure 2b, we can see that all wall types have two adsorption peaks, and the horizontal graphene sheet **Gh** has the highest

https://doi.org/10.1021/acsomega.3c05522
ACS Omega 2023, 8, 46577−46588

adsorption peak and the strongest adsorption ability for methane, and the curve decreases to 0 quickly ($y \approx \pm$ 2.0 Å) when y approaches the wall surface ($y = \pm$ 5.0 Å), the reason why **Gh** has a stronger attraction to methane is because of the deeper energy valley ϵ between the C_{Aro} atom and CH_4 united atom, which can be seen in Table 1, and Gh has more C_{Aro} on the wall surface, and with a higher carbon surface density than other wall types, and this can be seen in Figure S11 in the SI. The horizontal parallel stacking wall (**Ph**) has the second largest adsorption strength, and its peak height is lowered and the distribution is wider than those of **Gh**. **P0** and **O0** are located further to the center and have similar adsorption strength, but the $\rho(y)$ curve shows different properties: in **P0**, the location of peaks are closer to the center, and the $\rho(y)$ curve does not decrease to 0 when close to the wall surface at $y = \pm$ 5.0 Å; this is because that aromatic units are parallel stack in **P0**, so it has deeper grooves than that of **O0**, and a deeper groove could provide more space for methane, so that the $\rho(y)$ in **P0** is higher than **O0** at the wall surface when $y = \pm$ 5.0 Å.

From Figure 2c,d, we can see that when the slit size increases, adsorption peaks locate further to each other; they are still distributed close to the wall surface; and secondary peaks emerge out. The $\rho(y)$ is flat in the middle of the slit, meaning that the shale gas in the center is close to the bulk state. The order of adsorption strength we observed in s = 10 Å remains in the cases of s = 30 and 60 Å, where **Gh** > **Ph** > **P0** ≈ **O0**.

3.2. $\pi-\pi$ Stacking Affects Shale Gas Density Ratio. The density of methane inside the nanopore can be defined as $\rho = M/V$, where M is the total mass of methane in the nanopore, and V represents the volume. Previous research shows that under the same pressure, the density of methane increases as the nanopore size decreases. To quantify this change in densities, we use the density ratio $\rho_{d.r.}$, which is defined as $\rho_{d.r.} = \rho/\rho_{bulk}$, where ρ is the density of methane in the nanoslit we simulated, and ρ_{bulk} represents the density of methane in bulk state under the same pressure.

Figure 3 shows the density ratios for different wall types and slit sizes. We can see that for all wall types, as the slit size increases, their $\rho_{d.r.}$ decreases, meaning that under the same pressure, nanopores with smaller sizes could contain relatively more methane molecules and shale matrix with more smaller nanopores could have larger total shale gas storage. This observation is consistent with previous studies.[56] The reason why smaller nanopores have higher $\rho_{d.r.}$ is due to the high density adsorption peak; the smaller the pore sizes, the larger the volume ratio the peak will occupy inside the nanopore, resulting in a higher overall density.

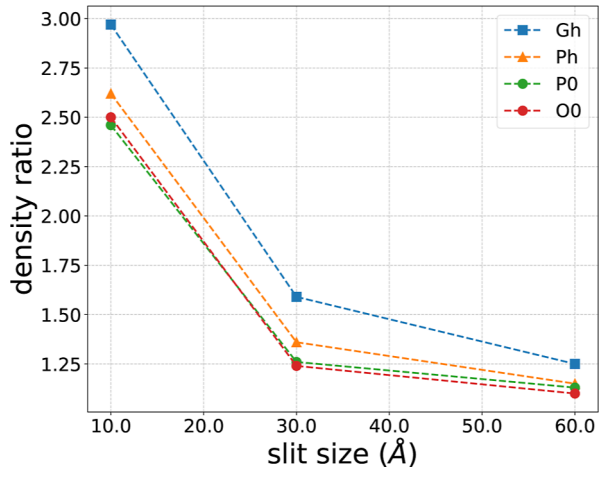

Figure 3. Density ratio of methane in four typical wall types: **Gh**, **Ph**, **P0**, and **O0**, and in different slit sizes.

From Figure 3, we can see that **Gh** has the highest density ratio and **Ph** has the second largest density ratio, while **P0** and **O0** have similar density ratios; this means that the smoother the nanopore surface the larger the density, and the trend of the density ratio is consistent with their methane adsorption abilities.

Besides the size of the nanoslit, pressure also has significant impact toward density ratio, we compute the density ratio of methane in nanoslit with s = 30 Å and pressure = 5, 20, and 60 MPa, the result is shown in Figure S9, the relation that **Gh** > **Ph** > **P0** ≈ **O0** still remains under different pressures, but the density ratio decreases as the pressure increases.

3.3. 2D Adsorption Free Energy. Different $\pi-\pi$ stacking structures not only affect the methane adsorption peak in $\rho(y)$ curve but will also have different 2D free energy profiles in the $x-z$ space. We calculate the methane adsorption density, $\rho(x, z)$ in the $x-z$ plan within the layer with a thickness of 5.0 Å near each wall. Then, the 2D methane adsorption free energy $F(x, y)$ can be obtained through $F(x, z) = -k_B T \ln\rho(x, z) + C$, where k_B is the Boltzmann constant, C is an arbitrary constant, which is chosen such that the highest free energy to be 0.

Figure 4 shows the 2D adsorption free energy of four typical wall types, and the $F(x, z)$ values are all scaled in the range of $-2.0k_BT \sim 0.0k_BT$. Figure 4a shows the $F(x, z)$ for **Gh**, and we can see that in the scale of $-2.0-0.0k_BT$, the free energy is quite smoothly and uniformly distributed, meaning that the roughness of the horizontal graphene type (**Gh**) is very small. Figure 4b,c,d shows the 2D free energy distribution for **Ph**, **P0**, and **O0**. We can see that the $F(x, z)$ are heterogeneously distributed and match with the patters of their $\pi-\pi$ stacking configurations. Their $F(x, z)$ values are ranging from -2.0 to $0.0k_BT$, indicating that the roughness are higher than that of **Gh**. 2D adsorption free energies of other wall types can be found in the Supporting Information.

3.4. $\pi-\pi$ Stacking Affects Shale Gas Transport Velocity. Methane flow properties are also crucial to the shale gas discovery; to simulate the methane flow in the nanoslit in the z direction, we use EF-NEMD by adding each methane molecule a constant force f = 0.001(kcal/mol)/Å in the z direction. The flow velocity increases from 0.0 Å/ps as time goes on; after 1.0 ns of simulation, the flow becomes stable and the velocity remains a constant.

Figure 5a shows the velocity of the methane flow at different y coordinates for type **Ph** with three slit sizes. We can see that the velocity curve $v_z(y)$ is in a parabola shape, with the maximum velocity appears at the center of the slit, while the velocity is zero when approaching the wall surface, this behavior is observed by several other research studies.[47,49,75] When the slit size increases from 10 to 60 Å, the peak velocity increases; this is also shown by Chen et al.[47] For other wall types, velocity profiles are all similar to those in Figure 5a.

Figure 5b compares peak velocities for all wall types with slit size of 30 Å, we can see that the velocity varies significantly in different wall types with different $\pi-\pi$ stacking orientations. **Gh** is much smoother than the rest of the wall structures, and its velocity is significantly higher and is shown in the figure with a broken y-axis. **Ph** and **O90** both have high velocities. Interestingly, with the same offset stacked columns as in **O90**, different orientations in **O0** and **O180** make the velocity drop

https://doi.org/10.1021/acsomega.3c05522
ACS Omega 2023, 8, 46577−46588

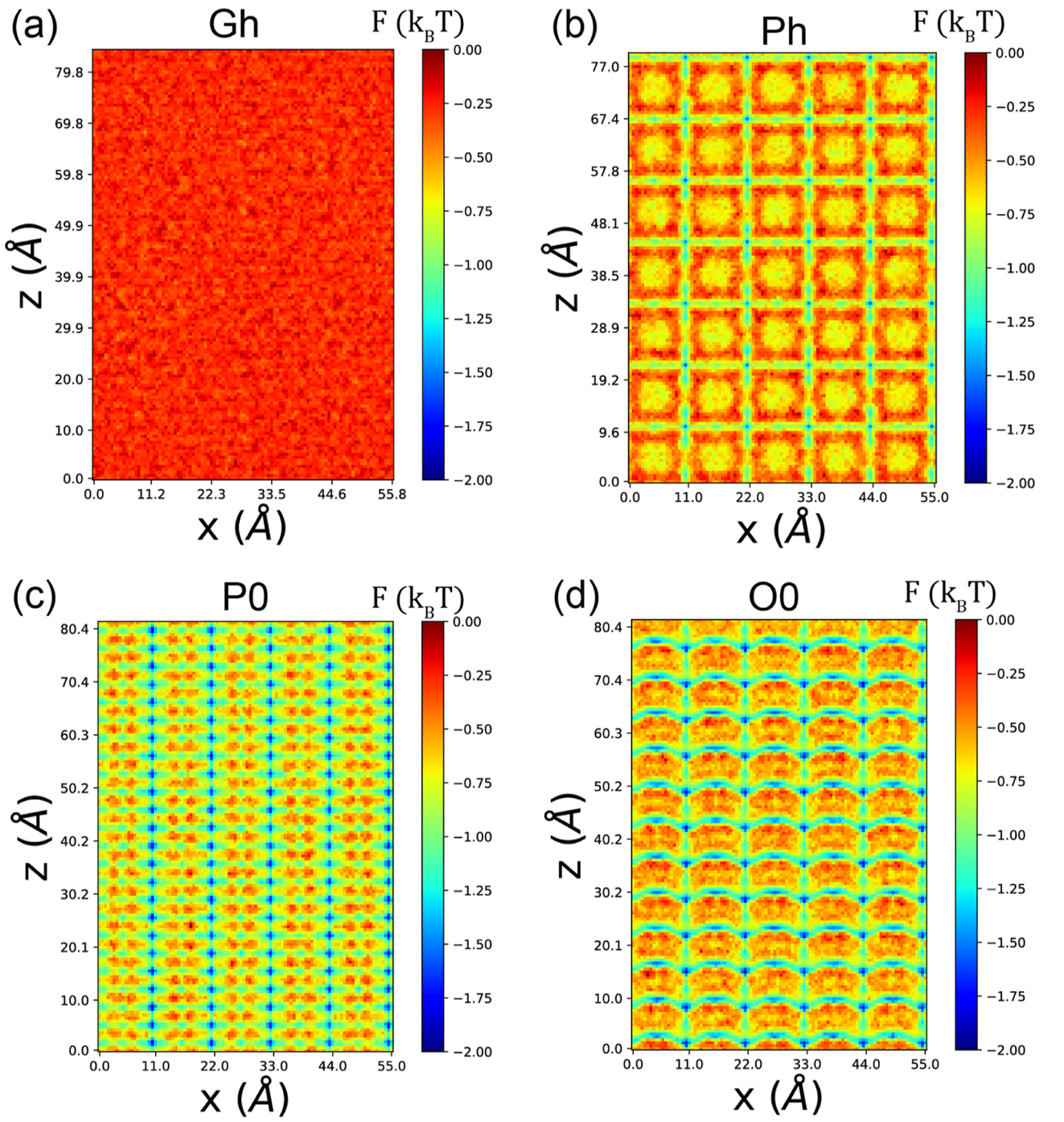

Figure 4. 2D methane adsorption free energy $F(x, z)$ for different wall types: (a) **Gh**, (b) **Ph**, (c) **P0**, and (d) **O0**. All $F(x, z)$ are colored with the range $-2.0k_BT \sim 0.0k_BT$.

down significantly. These observations indicate that both $\pi-\pi$ stacking type and orientation affect the flow velocity.

3.5. Shale Gas Flow Affects Adsorption Behavior. Figure 6 shows the comparison of the methane adsorption probability density $\rho(y)$ between the simulation with f = 0.0 (kcal)/mol/Å and f = 0.001 (kcal)/mol/Å for four typical wall types when the slit size equals 3.0 Å. We can see that the $\rho(y)$ curve does not change when the external force is turned on; this means that in the nanoslit we construct, the flow of methane does not affect the adsorption, regardless of the $\pi-\pi$ stacking type or orientation.

3.6. $\pi-\pi$ Stacking Affects Shale Gas Flow Flux. The flow flux is defined as the number of methane molecules that pass across the cross section of the nanoslit per unit time. We calculate the flow flux for all wall types with a slit size of 30.0 Å. All flux values are displayed in the bar plot in Figure 7. We can see that the order of the flux is mostly consistent with the order of the peak velocities (Figure 5b). However, a change needing to be noticed is that the flux of the **Ph** is more significantly higher than the rest of wall structures (except for **Gh**). This is because that the flux depends not only on the flow velocity but also on the density distribution of the methane, as can be seen in Figure 2b, the adsorption peak of **Ph** is taller and are more close to the

https://doi.org/10.1021/acsomega.3c05522
ACS Omega 2023, 8, 46577−46588

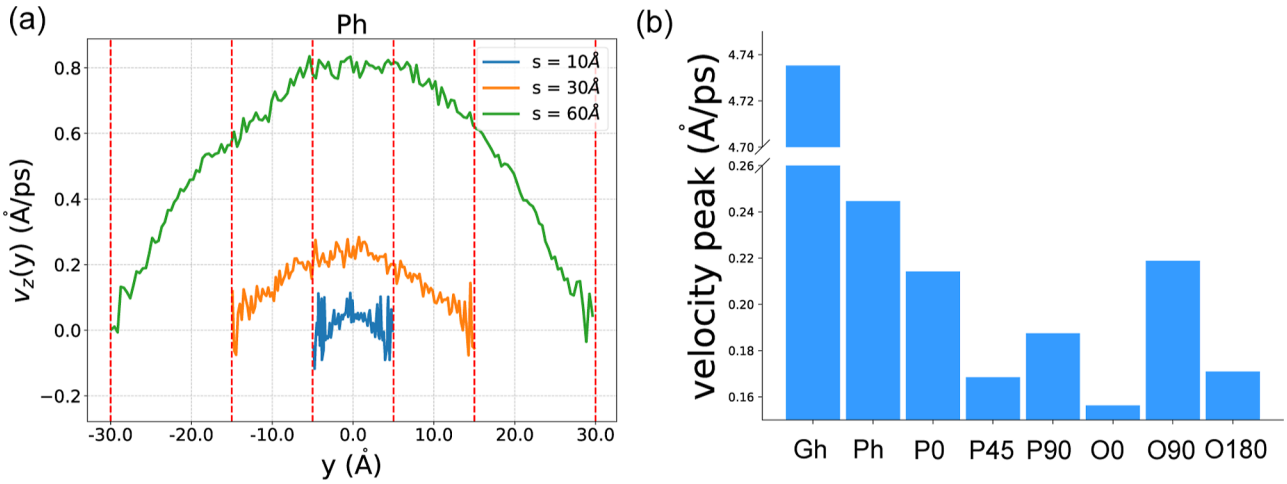

Figure 5. (a) Methane flow velocity $v_z(y)$ in the z direction as a function of y coordinate, with three slit sizes **Ph**. Red vertical dashed lines indicate boundaries of each nanoslit. (b) Peak velocities for different wall types with a slit size of 30 Å. Error bars of each data point is too small so that they are invisible.

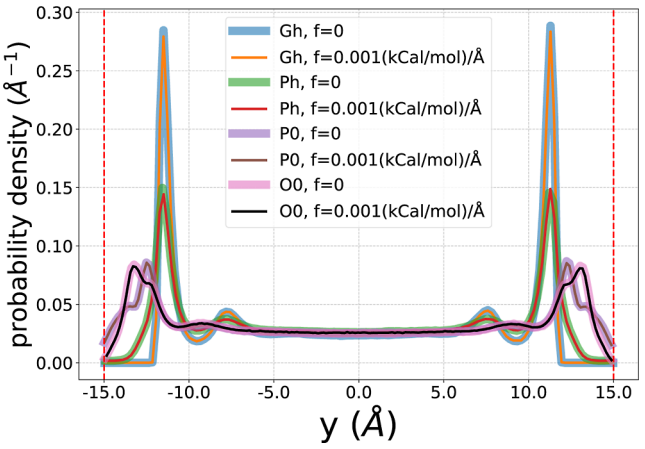

Figure 6. Comparison of the methane adsorption probability density over y axis with f = 0.0 (kcal/mol)/Å and f = 0.001 (kcal/mol)/Å.

center of the slit, and the parabola-shaped flow velocity is also larger in the center of the slit, these two factors make **Ph** have a relatively larger flux. In other words, in nanoslit **Ph**, there are more methane molecules in the center region and with higher velocities.

To explain the phenomena why different orientations of stacked columns have different flux behaviors, a "directional roughness" of the surface can be defined relative to the z direction. Traditionally, roughness is defined as the standard deviation of the potential energy over the 2D surface,[76] but this definition is isotropic and ignores the special direction of the flow. The "directional roughness" of the surface in the direction of z is defined by first calculating the standard deviation σ of the free energy $F(x, z)$ for strips along the z direction, and then, final "directional roughness" is obtained by taking the average of σs over all strips. For more detailed information about the definition and calculation of the directional roughness, please refer to the Supporting Information.

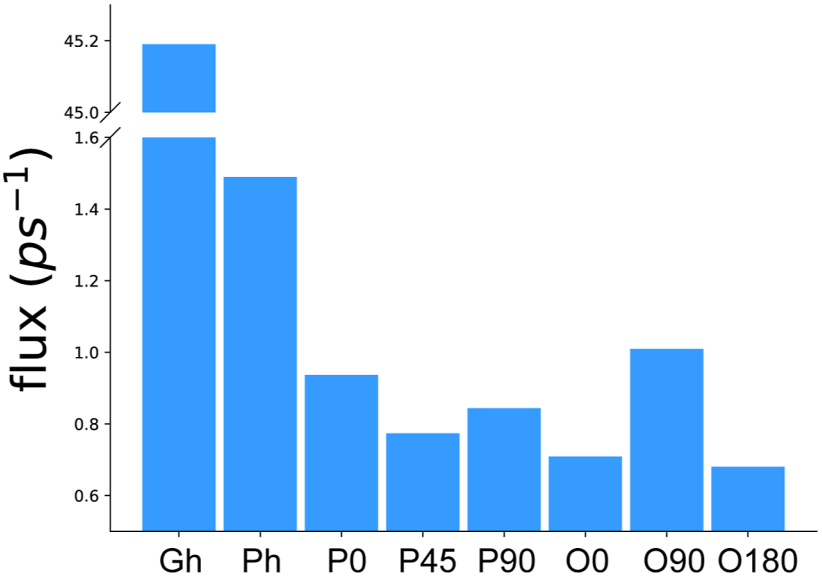

Figure 7. Flow flux for all wall types with different $\pi-\pi$ stacking configurations.

https://doi.org/10.1021/acsomega.3c05522
ACS Omega 2023, 8, 46577−46588

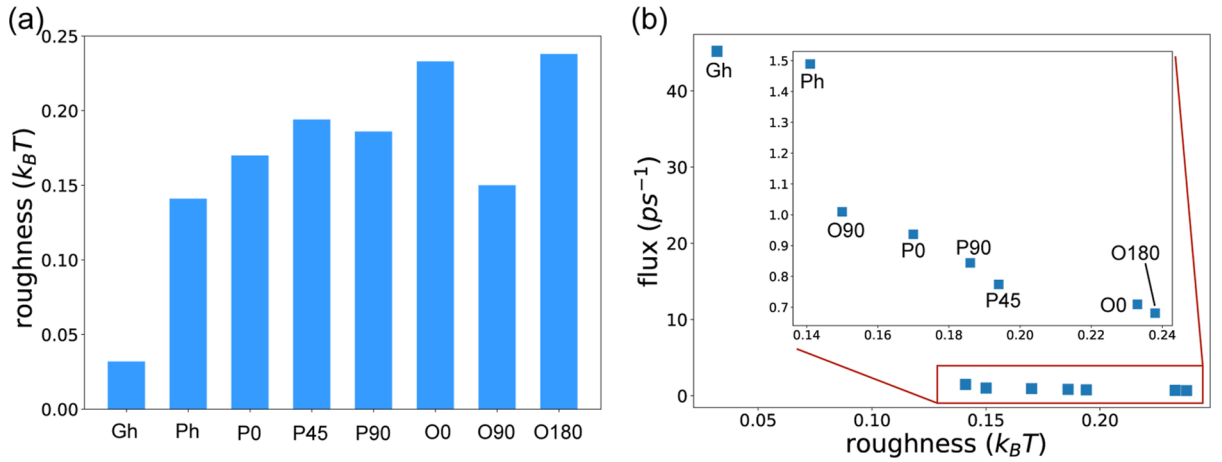

Figure 8. (a) Directional roughness relative to the z direction for all types of nanoslit. (b) The relationship between the methane flux and the directional roughness for all types of nanoslit.

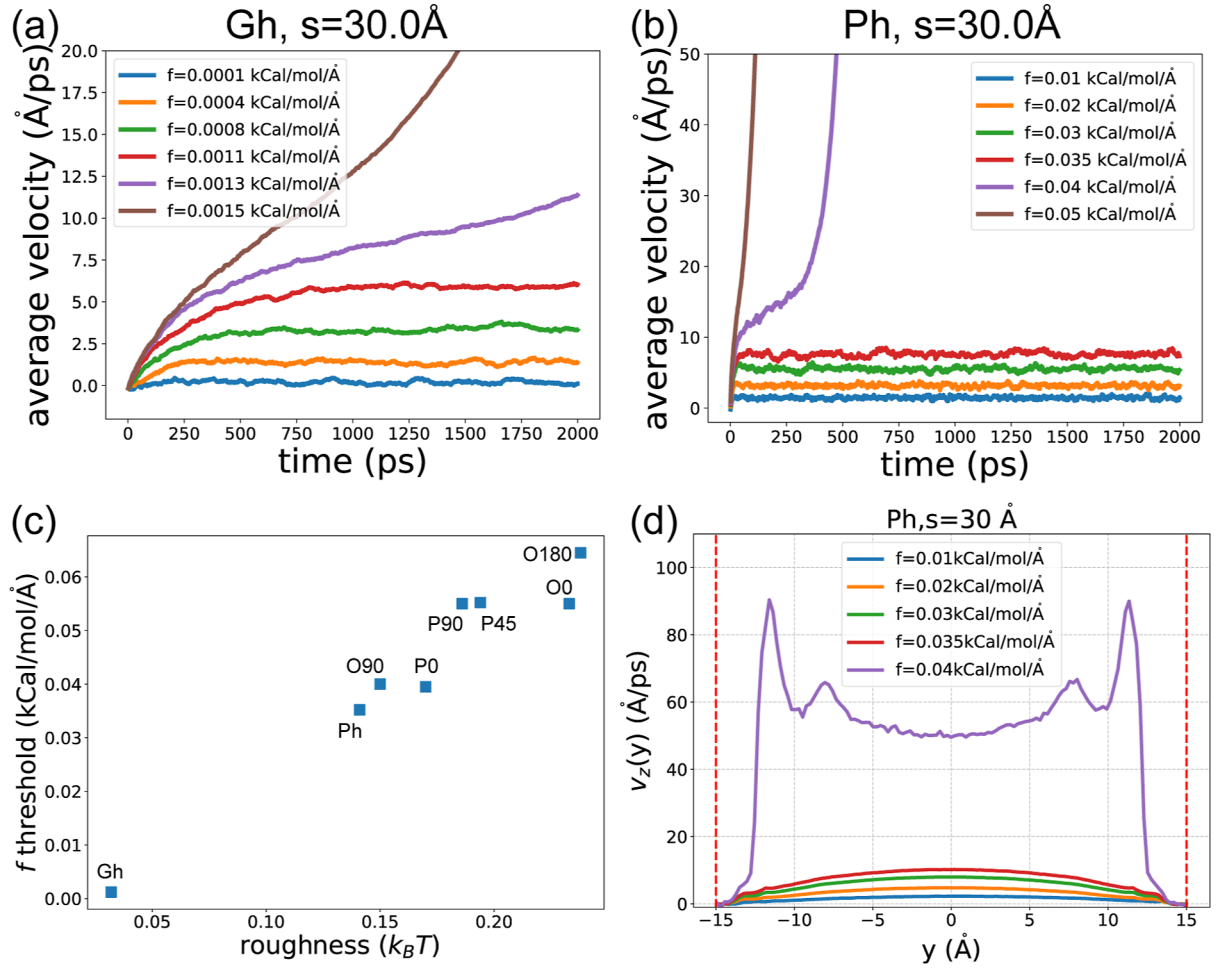

Figure 9. Average methane flow velocity as a function of time under different external forces with s = 30.0 Å for **Gh** (a) and **Ph** (b). (c) Relations between force threshold and directional roughness. (d) Methane flow velocity distribution in the y direction under different external forces for **Ph** and s = 30.0 Å.

Figure 8a shows the directional roughness for all wall types, and Figure 8b shows the relations between the directional roughness and the flux. We can see that as the roughness increases, the flow flux decreases monotonically and the Pearson correlation between the two variables is −0.85, meaning that they are mostly negatively correlated to each other. Noticeably, **Gh** is the smoothest wall type among all, resulting in the highest flux, and it has the smallest roughness value. From the same offset stacked columns, different orientations of the axle will result in quite different roughness and flux among **O0**, **O90**, and **180**, this means that the "directional roughness" we defined is a

https://doi.org/10.1021/acsomega.3c05522
ACS Omega 2023, 8, 46577−46588

good metric which nicely captures characteristics of flow flux and the "directional properties" of a rough surface.

We have also compute the self-diffusion coefficient D of methane molecules in the z direction when external force is turned off, as shown in Figure S10, we can see that D and roughness are not correlate to each other because D will be affected not only by the diffusion of the methane but also by the adsorption density, and methane molecules will collide with each other near the surface, the higher the density, the less mobility methane could have.

3.7. External Force Affects Methane Transport Behavior. We investigate the impact of external force f toward the methane transport behavior in the nanochannel by increasing f from small values to large values. We calculate the average velocities of methane in nanopores as a function of time under different f values, as shown in Figure 9a,b, for **Gh** and **Ph**, respectively. We can see that when f is small (under some threshold), the average velocities increase as time goes on and finally reach a plateau; this means that the flow velocity in the nanopore becomes a stable constant and will not increase further. As f increases, this velocity plateau also become higher. However, when f exceeds the threshold, the flow velocity cannot be flattened out but will increase linearly with time, and finally the simulation diverges. From Figure 9a,b, we could see that the force threshold for **Gh** is about $f = 0.0011$ (kcal)/mol/Å and $f = 0.035$ (kcal)/mol/Å for **Ph**.

When the external force f exceeds the threshold, the friction near the wall seems to disappear so that the methane flow will increase with no impedance, and this can be explained as follows: the potential P near the wall surface is rugged and not smooth, as shown in Figure 10. The potential surface will

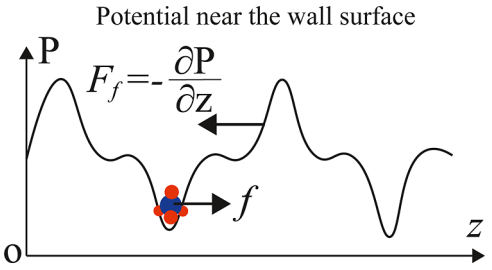

Figure 10. Schematic diagram showing the rugged potential near the wall surface, methane molecule is exerted by an external force f and suffers a frictional force $F_f = -\frac{\partial P}{\partial z}$.

provide the friction $F_f = -\frac{\partial P}{\partial z}$ to hinder the methane from moving in the z direction at the wall. In EF-NEMD simulation, each methane molecule is exerted with an external force f, and if f is small and less than F_f, friction will still take effect, since the methane molecule near the surface could not overcome the potential barrier, so that the velocity at the surface is 0, and the whole velocity distribution is parabola shaped. However, if f is larger than the threshold and overwhelm F_f, it could make methane near the surface be able to cross the potential barrier, so they could also be accelerated in the z direction, the flow velocity will not be 0 anymore. In this case, the velocity will increase linearly with time because external force f is a constant, which results in a constant acceleration. However, this "everlasting" acceleration will not happen in real kerogen nanochannels, because all realistic nanochannels have finite length, after a short period time of acceleration, methane will reach the end and stop accelerating, only in our simulation box with a periodic boundary condition in the z direction, this makes the box length equivalently infinite long, and the "everlasting" acceleration will happen.

To verify the above explanation about the existence of the force threshold, we find out thresholds for all wall types and display their relations with the directional roughness we calculated in Section 3.6. As shown in Figure 9c, roughness and force threshold are almost correlated with each other: surface with larger roughness will be more rugged, and the friction F_f is larger, so that the threshold is also larger; this is consistent with the explanation. Notice that horizontal graphene (**Gh**) is much smoother than the rest of walls, so its roughness and f threshold are both smaller significantly. We also calculate the velocity distribution in the y direction for **Ph** using the data from first 2 ns, as shown in Figure 9d, when f is smaller than the threshold, $v_z(y)$ is parabola-shaped distributed, and becomes higher as f increases, but when f exceeds the threshold, it is no longer parabola-shaped distributed, the velocity near the surface is high and not 0 anymore, this is also consistent with the above explanation. This finding could provide a potential method to enhance flow transport efficiency by increasing the pressure gradient along the flow direction, so that the molecule could overcome the potential barrier near the rough wall, and this would increase the flow velocity.

4. CONCLUSIONS

In this research, we utilized MD simulation to investigate how different $\pi-\pi$ stacking configurations will impact shale gas adsorption and transport in nanochannels. The configuration parameters include the orientation of the stacked column, the parallel or offset stacking type, and the size of the nanoslit. The following key conclusions could be drawn from this research.

Different wall types of nanoslit result in different methane adsorption probability density distributions; smoother wall structures have stronger adsorption strength, and the adsorption peaks are closer to the center of the channel. The density ratio is dependent on the wall types and slit sizes; smoother and narrower nanochannels have higher density ratio.

2D adsorption free energies are obtained for different wall types. Wall constituting of single graphene sheet has a flat free energy profile, while other wall types have heterogeneous free energy distributions, which match with the patterns of the stacked aromatic units.

Flow velocity depends on the slit size and wall types. The velocity across the nanoslit is parabola-shaped. The highest velocity appears at the center of the channel, and channels with larger sizes have higher velocities. Generally, smoother walls have higher velocities, and the velocity significantly depends on the orientation of the stacked columns. The existence of the nanoflow does not change the adsorption probability distribution.

Flow flux depends not only on velocity but on the density distribution, horizontally aligned parallel stacked columns (**Ph**) has higher methane density close to the center, where the velocity is also higher, making **Ph** has the highest flow flux. A concept of "directional roughness" is proposed and defined, which could well capture the directional properties of a rough surface, and it is negatively correlated with the flux.

When the external force is larger than the force threshold, methane molecules at the wall surface will be able to cross the potential barrier, and the methane flow velocity will not reach a plateau but will increase continuously as time goes on.

https://doi.org/10.1021/acsomega.3c05522
ACS Omega 2023, 8, 46577−46588

This research is helpful for understanding shale gas properties in a shale matrix and provides useful insights on nanoflow behaviors in other porous materials containing $\pi-\pi$ stackings.

■ ASSOCIATED CONTENT

Supporting Information

The Supporting Information is available free of charge at https://pubs.acs.org/doi/10.1021/acsomega.3c05522.

Definition and calculation of directional roughness; details of the MD simulation; visualization of all nanoslits from *x*, *y*, and *z* directions; 2D adsorption free energies for **P45**, **P90**, **O90**, and **O180**; density ratio under different pressures; self-diffusion coefficient for different walls; and calculation of carbon atom surface density (PDF)

■ AUTHOR INFORMATION

Corresponding Author

Jiang Wang − *College of Science, Guizhou Institute of Technology, Guiyang, Guizhou 550003, China;* orcid.org/0000-0002-3871-598X; Phone: 86-0851-86871682; Email: cwangjiang@git.edu.cn

Authors

Fuye Chen − *College of Science, Guizhou Institute of Technology, Guiyang, Guizhou 550003, China*

Jiaxuan Tang − *College of Science, Guizhou Institute of Technology, Guiyang, Guizhou 550003, China*

Complete contact information is available at: https://pubs.acs.org/10.1021/acsomega.3c05522

Notes

The authors declare no competing financial interest.

■ ACKNOWLEDGMENTS

This material was based upon work supported by Guizhou Provincial Science and Technology Projects (Grant no. Qian Ke He Ji Chu-ZK [2022] Yi Ban 183).

■ REFERENCES

(1) Wang, Q.; Li, R. Research status of shale gas: A review. *Renew. Sustain. Energy Rev.* **2017**, *74*, 715−720.

(2) Yang, Y.; Wang, L.; Fang, Y.; Mou, C. Integrated value of shale gas development: A comparative analysis in the United States and China. *Renew. Sustain. Energy Rev.* **2017**, *76*, 1465−1478.

(3) Middleton, R. S.; Gupta, R.; Hyman, J. D.; Viswanathan, H. S. The shale gas revolution: Barriers, sustainability, and emerging opportunities. *Appl. Energy* **2017**, *199*, 88−95.

(4) Paylor, A. The social−economic impact of shale gas extraction: a global perspective. *Third World Q* **2017**, *38*, 340−355.

(5) Wang, Y.; Chung, S. H. Soot formation in laminar counterflow flames. *Prog. Energy Combust. Sci.* **2019**, *74*, 152−238.

(6) Bowman, C. T. Control of combustion-generated nitrogen oxide emissions: technology driven by regulation. *Symp. (Int.) Combust., [Proc.]* **1992**, *24*, 859−878.

(7) Hill, D. G.; Nelson, C. Gas productive fractured shales: an overview and update. *GasTIPS* **2000**, *6*, 4−13.

(8) Curtis, J. B. Fractured shale-gas systems. *AAPG Bull.* **2002**, *86*, 1921−1938.

(9) Sondergeld, C. H.; Newsham, K. E.; Comisky, J. T.; Rice, M. C.; Rai, C. S. Petrophysical considerations in evaluating and producing shale gas resources. *SPE Unconventional Gas Conference*; Onepetro, 2010.

(10) Vandenbroucke, M.; Largeau, C. Kerogen origin, evolution and structure. *Org. Geochem.* **2007**, *38*, 719−833.

(11) Ungerer, P.; Collell, J.; Yiannourakou, M. Molecular modeling of the volumetric and thermodynamic properties of kerogen: Influence of organic type and maturity. *Energy Fuels* **2015**, *29*, 91−105.

(12) Mastalerz, M.; He, L.; Melnichenko, Y. B.; Rupp, J. A. Porosity of coal and shale: Insights from gas adsorption and SANS/USANS techniques. *Energy Fuels* **2012**, *26*, 5109−5120.

(13) Xu, H. Probing nanopore structure and confined fluid behavior in shale matrix: A review on small-angle neutron scattering studies. *Int. J. Coal Geol.* **2020**, *217*, 103325.

(14) Wang, Y.; Zhu, Y.; Chen, S.; Li, W. Characteristics of the nanoscale pore structure in Northwestern Hunan shale gas reservoirs using field emission scanning electron microscopy, high-pressure mercury intrusion, and gas adsorption. *Energy Fuels* **2014**, *28*, 945−955.

(15) Clarkson, C. R.; Solano, N.; Bustin, R. M.; Bustin, A.; Chalmers, G. R.; He, L.; Melnichenko, Y. B.; Radliński, A.; Blach, T. P. Pore structure characterization of North American shale gas reservoirs using USANS/SANS, gas adsorption, and mercury intrusion. *Fuel* **2013**, *103*, 606−616.

(16) Liu, X.; Nie, B.; Wang, W.; Wang, Z.; Zhang, L. The use of AFM in quantitative analysis of pore characteristics in coal and coal-bearing shale. *Mar. Petrol. Geol.* **2019**, *105*, 331−337.

(17) Afsharpoor, A.; Javadpour, F. Liquid slip flow in a network of shale noncircular nanopores. *Fuel* **2016**, *180*, 580−590.

(18) Loucks, R. G.; Reed, R. M.; Ruppel, S. C.; Hammes, U. Spectrum of pore types and networks in mudrocks and a descriptive classification for matrix-related mudrock pores. *AAPG Bull.* **2012**, *96*, 1071−1098.

(19) Guo, C.; Xu, J.; Wu, K.; Wei, M.; Liu, S. Study on gas flow through nano pores of shale gas reservoirs. *Fuel* **2015**, *143*, 107−117.

(20) Kaiser, M. J. Profitability assessment of Haynesville shale gas wells. *Energy* **2012**, *38*, 315−330.

(21) Javadpour, F.; Fisher, D.; Unsworth, M. Nanoscale gas flow in shale gas sediments. *J. Can. Petrol. Technol.* **2007**, *46*..

(22) Yin, Y.; Qu, Z.; Zhang, J. An analytical model for shale gas transport in kerogen nanopores coupled with real gas effect and surface diffusion. *Fuel* **2017**, *210*, 569−577.

(23) Huang, S.; Ma, X.; Yang, H.; Wu, J.; Zhang, J.; Zhao, S.; Zhang, D.; Ren, C.; Huang, L. Experimental characterization and molecular modeling of kerogen in Silurian deep gas shale from southern Sichuan Basin, China. *Energy Rep.* **2022**, *8*, 1497−1507.

(24) Rezlerová, E.; Brennan, J. K.; Lísal, M. Methane and carbon dioxide in dual-porosity organic matter: Molecular simulations of adsorption and diffusion. *AIChE J.* **2021**, *67*, No. e16655.

(25) Huang, L.; Ning, Z.; Wang, Q.; Qi, R.; Li, J.; Zeng, Y.; Ye, H.; Qin, H. Thermodynamic and structural characterization of bulk organic matter in Chinese Silurian shale: experimental and molecular modeling studies. *Energy Fuels* **2017**, *31*, 4851−4865.

(26) Kashinath, A.; Szulczewski, M. L.; Dogru, A. H. Modeling the effect of maturity on the elastic moduli of kerogen using atomistic simulations. *Unconventional Resources Technology Conference*; Onepetro: Denver, CO, 22−24 July 2019, 2019; pp 391−406.

(27) Wang, X.; Zhu, Y.; Liu, Y.; Li, W. Molecular Structure of Kerogen in the Longmaxi Shale: Insights from Solid State NMR, FT-IR, XRD and HRTEM. *Acta Geol. Sin. (Engl. Ed.)* **2019**, *93*, 1015−1024.

(28) Deng, J.-H.; Luo, J.; Mao, Y.-L.; Lai, S.; Gong, Y.-N.; Zhong, D.-C.; Lu, T.-B. π-π stacking interactions: Non-negligible forces for stabilizing porous supramolecular frameworks. *Sci. Adv.* **2020**, *6*, No. eaax9976.

(29) Heinz-yyyyyyKunert, S. L.; Pandya, A.; Dang, V. T.; Tran, P. N.; Ghosh, S.; McElheny, D.; Santarsiero, B. D.; Ren, Z.; Nguyen, A. I. Assembly of π-stacking helical peptides into a porous and multivariable proteomimetic framework. *J. Am. Chem. Soc.* **2022**, *144*, 7001−7009.

(30) Nichols, P. J.; Raston, C. L.; Steed, J. W. Engineering of porous π-stacked solids using mechanochemistry. *Chem. Commun.* **2001**, 1062−1063.

(31) Chen, C.; Di, Z.; Li, H.; Liu, J.; Wu, M.; Hong, M. An Ultrastable $\pi-\pi$ Stacked Porous Organic Molecular Framework as a Crystalline Sponge for Rapid Molecular Structure Determination. *CCS Chem.* **2022**, *4*, 1315−1325.

(32) Wang, J.; Ferguson, A. L. Mesoscale simulation of asphaltene aggregation. *J. Phys. Chem. B* **2016**, *120*, 8016−8035.
(33) Mudoi, M. P.; Sharma, P.; Khichi, A. S. A review of gas adsorption on shale and the influencing factors of CH4 and CO2 adsorption. *J. Pet. Sci. Eng.* **2022**, *217*, 110897.
(34) Zhang, B.; Shan, B.; Zhao, Y.; Zhang, L. Review of formation and gas characteristics in shale gas reservoirs. *Energies* **2020**, *13*, 5427.
(35) Hou, P.; Ju, Y.; Gao, F.; Wang, J.; He, J. Simulation and visualization of the displacement between CO 2 and formation fluids at pore-scale levels and its application to the recovery of shale gas. *Int. J. Coal Sci. Technol.* **2016**, *3*, 351−369.
(36) Pang, W.; Wang, Y.; Jin, Z. Comprehensive review about methane adsorption in shale nanoporous media. *Energy Fuels* **2021**, *35*, 8456−8493.
(37) Striolo, A.; Cole, D. R. Understanding shale gas: Recent progress and remaining challenges. *Energy Fuels* **2017**, *31*, 10300−10310.
(38) Taghavinejad, A.; Sharifi, M.; Heidaryan, E.; Liu, K.; Ostadhassan, M. Flow modeling in shale gas reservoirs: A comprehensive review. *J. Nat. Gas Sci. Eng.* **2020**, *83*, 103535.
(39) Liu, Y.; Zhu, Y.; Li, W.; Xiang, J.; Wang, Y.; Li, J.; Zeng, F. Molecular simulation of methane adsorption in shale based on grand canonical Monte Carlo method and pore size distribution. *J. Nat. Gas Sci. Eng.* **2016**, *30*, 119−126.
(40) Lin, K.; Huang, X.; Zhao, Y.-P. Combining image recognition and simulation to reproduce the adsorption/desorption behaviors of shale gas. *Energy Fuels* **2020**, *34*, 258−269.
(41) Hansson, T.; Oostenbrink, C.; van Gunsteren, W. Molecular dynamics simulations. *Curr. Opin. Struct. Biol.* **2002**, *12*, 190−196.
(42) Müller-Plathe, F. A simple nonequilibrium molecular dynamics method for calculating the thermal conductivity. *J. Chem. Phys.* **1997**, *106*, 6082−6085.
(43) MacElroy, J. Nonequilibrium molecular dynamics simulation of diffusion and flow in thin microporous membranes. *J. Chem. Phys.* **1994**, *101*, 5274−5280.
(44) Heffelfinger, G. S.; Swol, F. v. Diffusion in Lennard-Jones fluids using dual control volume grand canonical molecular dynamics simulation (DCV-GCMD). *J. Chem. Phys.* **1994**, *100*, 7548−7552.
(45) Collell, J.; Galliero, G.; Vermorel, R.; Ungerer, P.; Yiannourakou, M.; Montel, F.; Pujol, M. Transport of multicomponent hydrocarbon mixtures in shale organic matter by molecular simulations. *J. Phys. Chem. C* **2015**, *119*, 22587−22595.
(46) Yu, H.; Fan, J.; Xia, J.; Liu, H.; Wu, H. Multiscale gas transport behavior in heterogeneous shale matrix consisting of organic and inorganic nanopores. *J. Nat. Gas Sci. Eng.* **2020**, *75*, 103139.
(47) Chen, J.; Yu, H.; Fan, J.; Wang, F.; Lu, D.; Liu, H.; Wu, H. Channel-width dependent pressure-driven flow characteristics of shale gas in nanopores. *AIP Adv.* **2017**, *7*, 045217.
(48) Liu, B.; Qi, C.; Zhao, X.; Teng, G.; Zhao, L.; Zheng, H.; Zhan, K.; Shi, J. Nanoscale two-phase flow of methane and water in shale inorganic matrix. *J. Phys. Chem. C* **2018**, *122*, 26671−26679.
(49) Xu, H.; Yu, H.; Fan, J.; Zhu, Y.; Wang, F.; Wu, H. Two-phase transport characteristic of shale gas and water through hydrophilic and hydrophobic nanopores. *Energy Fuels* **2020**, *34*, 4407−4420.
(50) Hu, Y.; Devegowda, D.; Striolo, A.; Van Phan, A. T.; Ho, T. A.; Civan, F.; Sigal, R. Microscopic dynamics of water and hydrocarbon in shale-kerogen pores of potentially mixed wettability. *SPE J.* **2015**, *20*, 112−124.
(51) Yu, H.; Zhu, Y.; Jin, X.; Liu, H.; Wu, H. Multiscale simulations of shale gas transport in micro/nano-porous shale matrix considering pore structure influence. *J. Nat. Gas Sci. Eng.* **2019**, *64*, 28−40.
(52) Zhang, H.; Zeng, X.; Zhao, Z.; Zhai, Z.; Cao, D. Adsorption and selectivity of CH4/CO2 in functional group rich organic shales. *J. Nat. Gas Sci. Eng.* **2017**, *39*, 82−89.
(53) Xiong, J.; Liu, X.; Liang, L.; Zeng, Q. Methane adsorption on carbon models of the organic matter of organic-rich shales. *Energy Fuels* **2017**, *31*, 1489−1501.
(54) Song, W.; Yao, B.; Yao, J.; Li, Y.; Sun, H.; Yang, Y.; Zhang, L. Methane surface diffusion capacity in carbon-based capillary with application to organic-rich shale gas reservoir. *Chem. Eng. J.* **2018**, *352*, 644−654.
(55) Zhang, J.; Pei, G.; Zhang, L. Molecular dynamics simulation of methane gas flow in nanopores. *Petroleum* **2019**, *5*, 252−259.
(56) Sun, Z.; Li, X.; Liu, W.; Zhang, T.; He, M.; Nasrabadi, H. Molecular dynamics of methane flow behavior through realistic organic nanopores under geologic shale condition: Pore size and kerogen types. *Chem. Eng. J.* **2020**, *398*, 124341.
(57) Zhou, B.; Xu, R.; Jiang, P. Novel molecular simulation process design of adsorption in realistic shale kerogen spherical pores. *Fuel* **2016**, *180*, 718−726.
(58) Yu, K. B.; Bowers, G. M.; Loganathan, N.; Kalinichev, A. G.; Yazaydin, A. O. Diffusion behavior of methane in 3D kerogen models. *Energy Fuels* **2021**, *35*, 16515−16526.
(59) Swart, M.; van der Wijst, T.; Fonseca Guerra, C.; Bickelhaupt, F. M. π-π stacking tackled with density functional theory. *J. Mol. Model.* **2007**, *13*, 1245−1257.
(60) Claessens, C. G.; Stoddart, J. F. $\pi-\pi$ Interactions in self-assembly. *J. Phys. Org. Chem.* **1997**, *10*, 254−272.
(61) Chen, T.; Li, M.; Liu, J. $\pi-\pi$ stacking interaction: a nondestructive and facile means in material engineering for bioapplications. *Cryst. Growth Des.* **2018**, *18*, 2765−2783.
(62) Sentker, K.; Zantop, A. W.; Lippmann, M.; Hofmann, T.; Seeck, O. H.; Kityk, A. V.; Yildirim, A.; Schönhals, A.; Mazza, M. G.; Huber, P. Quantized self-assembly of discotic rings in a liquid crystal confined in nanopores. *Phys. Rev. Lett.* **2018**, *120*, 067801.
(63) Bhattacharjee, S.; Lugger, J. A.; Sijbesma, R. P. Tailoring pore size and chemical interior of near 1 nm sized pores in a nanoporous polymer based on a discotic liquid crystal. *Macromolecules* **2017**, *50*, 2777−2783.
(64) Lin, K.; Yuan, Q.; Zhao, Y.-P. Using graphene to simplify the adsorption of methane on shale in MD simulations. *Comput. Mater. Sci.* **2017**, *133*, 99−107.
(65) Delhaes, P. *Graphite and Precursors*; CRC Press, 2000.
(66) Plimpton, S. Fast parallel algorithms for short-range molecular dynamics. *J. Comput. Phys.* **1995**, *117*, 1−19.
(67) Thompson, A. P.; Aktulga, H. M.; Berger, R.; Bolintineanu, D. S.; Brown, W. M.; Crozier, P. S.; in't Veld, P. J.; Kohlmeyer, A.; Moore, S. G.; Nguyen, T. D.; et al. LAMMPS-a flexible simulation tool for particle-based materials modeling at the atomic, meso, and continuum scales. *Comput. Phys. Commun.* **2022**, *271*, 108171.
(68) Malde, A. K.; Zuo, L.; Breeze, M.; Stroet, M.; Poger, D.; Nair, P. C.; Oostenbrink, C.; Mark, A. E. An automated force field topology builder (ATB) and repository: version 1.0. *J. Chem. Theory Comput.* **2011**, *7*, 4026−4037.
(69) Koziara, K. B.; Stroet, M.; Malde, A. K.; Mark, A. E. Testing and validation of the Automated Topology Builder (ATB) version 2.0: prediction of hydration free enthalpies. *J. Comput. Aided Mol. Des.* **2014**, *28*, 221−233.
(70) Stroet, M.; Caron, B.; Visscher, K. M.; Geerke, D. P.; Malde, A. K.; Mark, A. E. Automated topology builder version 3.0: Prediction of solvation free enthalpies in water and hexane. *J. Chem. Theory Comput.* **2018**, *14*, 5834−5845.
(71) Van Der Spoel, D.; Lindahl, E.; Hess, B.; Groenhof, G.; Mark, A. E.; Berendsen, H. J. GROMACS: fast, flexible, and free. *J. Comput. Chem.* **2005**, *26*, 1701−1718.
(72) Chávez Thielemann, H.; Cardellini, A.; Fasano, M.; Bergamasco, L.; Alberghini, M.; Ciorra, G.; Chiavazzo, E.; Asinari, P. From GROMACS to LAMMPS: GRO2LAM: A converter for molecular dynamics software. *J. Mol. Model.* **2019**, *25*, 147.
(73) Schmid, N.; Eichenberger, A. P.; Choutko, A.; Riniker, S.; Winger, M.; Mark, A. E.; Van Gunsteren, W. F. Definition and testing of the GROMOS force-field versions 54A7 and 54B7. *Eur. Biophys. J.* **2011**, *40*, 843−856.
(74) Linstorm, P. NIST chemistry webbook, NIST standard reference database number 69. *J. Phys. Chem. Ref. Data, Monogr.* **1998**, *9*, 1−1951.
(75) Yu, H.; Xu, H.; Fan, J.; Zhu, Y.-B.; Wang, F.; Wu, H. Transport of shale gas in microporous/nanoporous media: molecular to pore-scale simulations. *Energy Fuels* **2021**, *35*, 911−943.

https://doi.org/10.1021/acsomega.3c05522
ACS Omega 2023, 8, 46577−46588

(76) Wang, G.; Ma, Y.; Zhao, Y.; Chen, W. Carbon Isotope Fractionation during Shale Gas Transport through Organic and Inorganic Nanopores from Molecular Simulations. *Energy Fuels* **2021**, *35*, 11992−12004.

https://doi.org/10.1021/acsomega.3c05522
ACS Omega 2023, 8, 46577−46588